AD

AD-A184 171

MEMORANDUM REPORT BRL-MR-3610

THREE DIMENSIONAL BASE FLOW CALCULATION FOR A PROJECTILE AT TRANSONIC VELOCITY

JUBARAJ SAHU

DTIC
ELECTE
SEP 0 8 1987
D

JUNE 1987

US ARMY BALLISTIC RESEARCH LABORATORY
ABERDEEN PROVING GROUND, MARYLAND

REPORT DOCUMENTATION PAGE

Form Approved
OMB No 0704-0188
Exp Date Jun 30, 1986

1a REPORT SECURITY CLASSIFICATION	1b. RESTRICTIVE MARKINGS
UNCLASSIFIED	

2a SECURITY CLASSIFICATION AUTHORITY	3 DISTRIBUTION/AVAILABILITY OF REPORT
2b DECLASSIFICATION/DOWNGRADING SCHEDULE	Approved for public release, distribution unlimited.

4 PERFORMING ORGANIZATION REPORT NUMBER(S)	5 MONITORING ORGANIZATION REPORT NUMBER(S)

6a NAME OF PERFORMING ORGANIZATION	6b OFFICE SYMBOL (If applicable)	7a NAME OF MONITORING ORGANIZATION
U.S. Army Ballistic Research Laboratory	SLCBR-LF-R	

6c ADDRESS (City, State, and ZIP Code)	7b ADDRESS (City, State, and ZIP Code)
Aberdeen Proving Ground, Maryland 21005-5066	

8a NAME OF FUNDING/SPONSORING ORGANIZATION	8b OFFICE SYMBOL (If applicable)	9 PROCUREMENT INSTRUMENT IDENTIFICATION NUMBER

8c ADDRESS (City, State, and ZIP Code)	10 SOURCE OF FUNDING NUMBERS			
	PROGRAM ELEMENT NO	PROJECT NO	TASK NO	WORK UNIT ACCESSION NO
	61102A	1L161102AH43	00	001 AJ

11 TITLE (Include Security Classification)

THREE DIMENSIONAL BASE FLOW CALCULATION FOR A PROJECTILE AT TRANSONIC VELOCITY

12 PERSONAL AUTHOR(S)
SAHU, JUBARAJ

13a TYPE OF REPORT	13b TIME COVERED	14 DATE OF REPORT (Year, Month, Day)	15 PAGE COUNT
Memorandum Report	FROM _____ TO _____		

16. SUPPLEMENTARY NOTATION

17	COSATI CODES		18 SUBJECT TERMS (Continue on reverse if necessary and identify by block number)	
FIELD	GROUP	SUB-GROUP	Base Flow	Navier-Stokes
01	01		Angle of Attack	Transonic Speed
19	04			

19. ABSTRACT (Continue on reverse if necessary and identify by block number) As part of an ongoing research program to develop predictive capabilities for projectile aerodynamics at transonic speeds, a three dimensional base flow code has been developed to compute the base region or wake flow behind projectile. The time-marching, thin-layer, Navier-Stokes computational technique has been used, in conjunction with a unique flow field segmentation procedure, to compute the full flow field over a projectile including the base region at angle of attack. A flow field solution has been obtained for a typical artillery projectile at Mach number, M = .96 and 4° angle of attack. Details of the flow field on the boattailed afterbody and in the base region are presented. Surface pressure, base pressure and aerodynamic coefficients are computed and compared with experiment.

20 DISTRIBUTION/AVAILABILITY OF ABSTRACT	21 ABSTRACT SECURITY CLASSIFICATION
☑ UNCLASSIFIED/UNLIMITED ☐ SAME AS RPT ☐ DTIC USERS	UNCLASSIFIED

22a NAME OF RESPONSIBLE INDIVIDUAL	22b TELEPHONE (Include Area Code)	22c OFFICE SYMBOL
JUBARAJ SAHU	(301) 278-3707	SLCBR-LF

DD FORM 1473, 84 MAR

83 APR edition may be used until exhausted
All other editions are obsolete

SECURITY CLASSIFICATION OF THIS PAGE

TABLE OF CONTENTS

Accession For

NTIS CRA&I

DTIC TAB

Unannounced

Justification

By

Distribution/

Availability

Dist

A-1

QUALITY INSPECTED 2

iii

LIST OF FIGURES

I. INTRODUCTION

The accurate prediction of projectile aerodynamics is of significant importance in the early design stage of a projectile. An area of considerable interest in transonic projectile aerodynamics is the determination of the critical aerodynamic behavior. The critical aerodynamic behavior of projectiles occurs in the transonic speed regime, $0.9 < M < 1.1$, where the aerodynamic coefficients have been found to increase by as much as 100%. This rapid change in the aerodynamic coefficients can be attributed in part to the complex flow structure existing on projectiles at transonic speeds. For projectiles flying at angle of attack, the shock pattern is asymmetric and thus, contributes to the critical aerodynamic behavior.

In recent years a considerable research effort has been focused on the development of modern predictive capabilities for determining projectile aerodynamics. Numerical capabilities have recently been developed using the Navier-Stokes computational technique to compute the flow over slender bodies of revolution at transonic speeds. This technique was used to predict projectile aerodynamics for both axisymmetric[1] and 3-D flow[2] situations. The 3-D flow predictions[2] were rather poor which could be due to lack of sufficient grid resolution and, more importantly, lack of correct base flow modeling. These calculations did not include the base region flow. The upstream effect the base region flow may have on the afterbody flow field and the associated shock structure was, thus, neglected. Deiwert[3] has also successfully computed the three dimensional flow field over a boattailed afterbody. Emphasis in his work was on the boattail flow field and not on the base region flow. Recently, an axisymmetric thin-layer Navier-Stokes base flow code has been developed to compute the entire projectile flow field including the base region using a unique flow field segmentation procedure.[4] This code has been used to compute base flow with and without mass injection[4] and including jet effects.[5] The objective of this initial effort is to extend the capability of this code to three-dimensions in order to include the upstream effect of the base flow and to calculate the pitch plane projectile aerodynamics at transonic speeds. The asymmetric shock pattern existing on the projectile and possible base region influence are felt to be the major contributors to the critical aerodynamic behavior at transonic speeds.

This report describes the initial capability which is used to predict the flow field over a 6 caliber secant-ogive-cylinder-boattail projectile at $M = .96$ and $\alpha = 4°$. Computed results, obtained on a Cray X-MP computer are presented and compared to experimental data. A brief description of the governing equations and the flow field segmentation procedure is included.

II. GOVERNING EQUATIONS

The Navier-Stokes equations solved herein make use of the thin-layer approximation.[6] That is, the viscous terms involving velocity gradients in both the longitudinal and circumferential directions are neglected. The viscous terms are retained, however, for velocity gradients in a direction nearly normal to the surface where large flow field gradients exist. This formulation retains the momentum equations in all three coordinate directions. The retention of the three momentum equations allows for the computation of separated flow and thus differs significantly from boundary-layer assumptions.

The equations solved here are written in a generalized coordinate system. This allows a wide variety of body shapes to be computed using the same basic numerical technique. The three-dimensional, transformed, thin-layer Navier Stokes equations written in nondimensional, strong conservation law form are[7]

$$\partial_\tau \hat{q} + \partial_\xi \hat{E} + \partial_\eta \hat{F} + \partial_\zeta \hat{G} = Re^{-1} \partial_\zeta \hat{S} \tag{1}$$

where generalized coordinates

$$\xi = \xi(x,y,z,t) \quad - \text{ longitudinal coordinate}$$

$$\eta = \eta(x,y,z,t) \quad - \text{ circumferential coordinate}$$

$$\zeta = \zeta(x,y,z,t) \quad - \text{ near normal coordinate}$$

$$\tau = t \quad\quad\quad\quad - \text{ time}$$

are used and

$$\hat{q} = J^{-1} \begin{bmatrix} \rho \\ \rho u \\ \rho v \\ \rho w \\ e \end{bmatrix} \quad\quad \hat{E} = J^{-1} \begin{bmatrix} \rho U \\ \rho u U + \xi_x p \\ \rho v U + \xi_y p \\ \rho w U + \xi_z p \\ (e+p)U - \xi_t p \end{bmatrix}$$

$$\hat{F} = J^{-1} \begin{bmatrix} \rho V \\ \rho u V + \eta_x p \\ \rho v V + \eta_y p \\ \rho w V + \eta_z p \\ (e+p)V - \eta_t p \end{bmatrix} \quad\quad \hat{G} = J^{-1} \begin{bmatrix} \rho W \\ \rho u W + \zeta_x p \\ \rho v W + \zeta_y p \\ \rho w W + \zeta_z p \\ (e+p)W - \zeta_t p \end{bmatrix}$$

2

$$\hat{S} = J^{-1} \begin{bmatrix} 0 \\ \mu(\zeta_x^2 + \zeta_y^2 + \zeta_z^2)u_\zeta + (\mu/3)(\zeta_x u_\zeta + \zeta_y v_\zeta + \zeta_z w_\zeta)\zeta_x \\ \mu(\zeta_x^2 + \zeta_y^2 + \zeta_z^2)v_\zeta + (\mu/3)(\zeta_x u_\zeta + \zeta_y v_\zeta + \zeta_z w_\zeta)\zeta_y \\ \mu(\zeta_x^2 + \zeta_y^2 + \zeta_z^2)w_\zeta + (\mu/3)(\zeta_x u_\zeta + \zeta_y v_\zeta + \zeta_z w_\zeta)\zeta_z \\ \{(\zeta_x^2 + \zeta_y^2 + \zeta_z^2)[0.5\mu(u^2 + v^2 + w^2)_\zeta + \kappa Pr^{-1}(\gamma - 1)^{-1}(a^2)_\zeta] \\ + (\mu/3)(\zeta_x u + \zeta_y v + \zeta_z w)(\zeta_x u_\zeta + \zeta_y v_\zeta + \zeta_z w_\zeta)\} . \end{bmatrix}$$

The velocities in the ξ, η, ζ coordinates are

$$U = \xi_t + \xi_x u + \xi_y v + \xi_z w$$
$$V = \eta_t + \eta_x u + \eta_y v + \eta_z w \qquad (2)$$
$$W = \zeta_t + \zeta_x u + \zeta_y v + \zeta_z w$$

which represent the contravariant velocity components.

The Cartesian velocity components (u, v, w) are retained as the dependent variables and are nondimensionalized with respect to a_∞ (the free stream speed of sound). The local pressure is determined using the relation

$$p = (\gamma - 1)[e - .5\rho(u^2 + v^2 + w^2)] \qquad (3)$$

where γ is the ratio of specific heats, density (ρ), is referenced to ρ_∞ and total energy (e) to $\rho_\infty a_\infty^2$.

III. NUMERICAL METHOD

1. COMPUTATIONAL ALGORITHM

The numerical scheme used for the solution of Equation (1) is a fully, implicit, approximately factored, finite difference algorithm in delta form as analyzed by Beam and Warming.[8] This scheme can be first- or second-order accurate in time and second- or fourth-order accurate in the three spatial directions. The solution of the three-dimensional equations is implemented by an approximate factorization which allows the system of equations to be solved in three one-dimensional steps. This procedure has been utilized in previous applications[2-9] with high degree of success. Additional details of the numerical method, computational algorithm and boundary conditions can be found in Reference 9.

3

2. FLOW FIELD SEGMENTATION

A unique flow field segmentation procedure has been used for three-dimensional flow over a projectile including the base flow. This is similar to the one previously used in the axisymmetric flow situation[4] where two 2-D adjoining grids were used. The segmentation process allowed the existing finite difference algorithm to be applied to two 3-D adjoining grids by making modifications in the internal structure of the block tridiagonal matrix and boundary conditions. This greatly simplified the development of the code for computations of flow over a projectile at angle of attack including the base region.

Figure 1 is a schematic illustration of the flow field segmentation used to compute the entire projectile flow field that includes the base flow. It shows how the two grids ABCD and AEFG in the physical plane are transformed into a single segmented grid in the computational domain. An important advantage of this segmentation procedure lies in the preservation of the sharp corner at the base, which allows easy blending of the computational meshes between the regions ABCD and AEFG. No approximation of the actual sharp corner at the base is made. Thus, realistic representation of the base is inherent in the current procedure. The cross-hatched region represents the projectile. The line BC is the projectile base and the region ABCD is the base or wake region. The line AB is a computational cut through the physical base region that acts as a repetitive boundary in the computational domain.

With the computational domain so segmented, implicit integration is carried out in ξ, ζ and η directions by solving the block tridiagonal matrices first in ξ and then in ζ and η. The block tridiagonal matrix in the ξ direction has elements at $J = JB$, $JB+1$ which are treated as internal boundaries in the computational domain ($J = JB$ represents the projectile base and $J = JB+1$ is the nose axis). The block tridiagonal matrix in the ξ direction takes the following form (after setting $\epsilon_I = 0$ to simplify the illustration)

$$
\begin{bmatrix}
 & I & & A_3 & & \\
-A_2 & & I & & A_4 & \\
 & \cdot & & \cdot & & \cdot \\
 & & \cdot & & \cdot & \\
 & \cdot & & \cdot & & \cdot \\
-A_{JB-2} & & I & & A_{JB} & \\
 & 0 & & I & & 0 \\
 & 0 & & I & & 0 \\
 & -A_{JB+1} & I & & A_{JB+3} & \\
 & & \cdot & \cdot & & \cdot \\
 & & \cdot & & \cdot & \\
 & & \cdot & \cdot & & \\
 & -A_{JMAX-2} & I & &
\end{bmatrix}
\begin{bmatrix}
\Delta q_2 \\
\Delta q_3 \\
\cdot \\
\cdot \\
\cdot \\
\Delta q_{JB} \\
\Delta q_{JB+1} \\
\cdot \\
\cdot \\
\cdot \\
\cdot \\
\Delta q_{JMAX-1}
\end{bmatrix}
=
\begin{bmatrix}
RHS_2 \\
RHS_3 \\
\cdot \\
\cdot \\
\cdot \\
0 \\
0 \\
\cdot \\
0 \\
\cdot \\
\cdot \\
RHS_{JMAX-1}
\end{bmatrix}
\tag{4}
$$

Here A's denote the quantity $\dfrac{\Delta t}{2\Delta \xi} \hat{A}$, I is a 5 × 5 identity matrix and RHS is the right hand side of the finite-difference form of Equation (1). Note the appearance of the uncoupled block tridiagonals. The rows at JB and JB+1 are

4

particularly simple because boundary conditions are updated explicitly at the end of inversions. One simply fills the block tridiagonal matrix ignoring the base JB and the nose axis JB+1. Elements in these rows are then overloaded as shown above. The flow field segmentation does not affect the block tridiagonal matrix in the ζ and η directions. This is readily accomplished by initially ignoring these boundaries and then overwriting the tridiagonal elements.

3. BOUNDARY CONDITIONS AND TURBULENCE MODEL

The no slip boundary condition for viscous flow is enforced by setting the contravariant velocities to zero, i.e.,

$$U = V = W = 0$$

on the projectile surface. The flow field in the immediate near-wake region has been considered to be weakly viscous and inviscid boundary condition is used at the base. The viscous terms near the projectile surface and across the shear layer are considered to be the most dominant and have been retained within the thin-layer approximation used here. This approximation neglects the viscous terms normal to the base that are believed to be less significant.

Recently, solutions have been obtained for axisymmetric base flow computations where viscous terms in the longitudinal direction or normal to the base were included. These unpublished results obtained with full Navier-Stokes equations and viscous boundary condition at the base are not found to be significantly different from the earlier solutions obtained with the thin-layer approximation and inviscid base boundary condition. This justifies our use of inviscid boundary condition at the base. Additionally, the grid points used for the three dimensional calculation results in a rather coarse grid in the near wake. The pressure, p is calculated using the three transformed momentum equations and density, ρ is extrapolated at the inner boundary (body surface). At the base, these two quantities are extrapolated.

At the outer boundary, constant free stream values are used for all variables. The flow variables above and below the cut (line AB in Figure 1) are simply averaged to determine the boundary conditions along the cut. All variables at the downstream, upstream axis and on the center line of the wake region are obtained through extrapolation. For nonspinning projectiles at angle of attack, symmetry exists about the axis of the projectile and the computation is performed only over the half plane. Thus, symmetry boundary conditions are imposed at both ends in the circumferential direction. Because of this boundary condition, only the static aerodynamic coefficients for pitch plane aerodynamics can be determined. For spinning projectiles at angle of attack, the full three dimensional flow field must be computed.

For the computation of turbulent flows, a turbulence model must be supplied. In the present calculations, a two-layer algebraic eddy viscosity model due to Baldwin and Lomax[6] is used. In their two-layer model, the inner region follows the Prandtl-Van Driest formulation. The outer formulation can be used in attached and separated boundary layers and with minor modifications in wakes as well. In both the inner and outer formulations, the distribution

5

of vorticity is used to determine the length scales, thereby avoiding the necessity of finding the outer edge of the boundary layer (or wake). For base or wake flow, a few minor modifications are made. These are discussed in Reference 4 and are not included here. The algebraic eddy viscosity model is simple to use; however, it is not strictly valid for such wake flows. Two equation turbulence models are better suited for these flows. These models have been used to compute axisymmetric base flow[10] and have failed to provide better predictions than those obtained with simple algebraic eddy viscosity model. Improvement in the advanced two-equation turbulence modeling is needed. The accuracy of the numerical computations should improve with improvement in the turbulence modeling.

IV. MODEL GEOMETRY AND EXPERIMENT

One means of establishing the computational accuracy of a numerical scheme is through comparisons with available experimental data. The model used for the experiment and computational study presented here is an idealization of a realistic artillery projectile geometry. The experimental model shown in Figure 2 consists of a three-caliber (1 caliber = maximum body diameter), sharp, secant-ogive nose, a two-caliber cylindrical midsection, and a one-caliber 7-deg conical afterbody or boattail. A similar model was used for the computational studies with the only difference being a 5% rounding of the nose tip. The nose tip rounding was done for computational efficiency and is considered to have little impact on the final integrated forces.

The experimental pressure data[11] [12] used for comparison in this report were obtained in the NASA Langley 8-ft Pressure Tunnel using a sting-mounted model. The test conditions of 1 atm supply pressure and 320 K supply temperature resulted in a Reynolds number of 4.5×10^6 based on model length. The pressure data were obtained with the model nonspinning.

V. RESULTS

As indicated earlier, this solution technique involves solving the time-dependent, thin-layer, Navier-Stokes equations. The procedure is started by assuming uniform free-stream conditions for all grid points in the computational domain. A slow start of the boundary conditions is implemented and the calculation marches in time until a steady-state solution is obtained. A criterion for convergence is for the solution residual to decrease by three orders of magnitude. Also, the surface pressure distribution is checked for time invariance. The implicit technique used here allows for large computational time steps to be taken, which helps to reduce the total computation time. All the computed results to be presented are for M = .96 and α = 4°.

One of the first steps in performing a computation is the generation of a computational grid. These points are determined prior to the computations and are not changed with time. An example of the computational grid used in this study is shown in Figure 3. This figure shows an expanded view of the grid for the boattailed afterbody and the base region. The surface of the boattail and the base can be seen along with the grids in the windward and leeward planes. These grids (excluding the base region) were generated using a modified version of an elliptic grid generation code described in Reference 13.

6

The grid in the base region was then added following the flowfield segmentation procedure to obtain the full grid. The outer flowfield boundary was placed approximately 18 body diameters from the body surface. At this distance, the flowfield should be uniform and the imposed free-stream boundary conditions are valid. The clustering of grid points near the body surface is required to resolve the viscous boundary layer near the body surface. Grid clustering has also been used in the longitudinal direction near the boattail and the base corners where large gradients in the flow variables are expected. The largest grid size that could be accommodated in the Cray X-MP/22 computer at NASA Ames Research Center was 70 X 36 X 21 (longitudinal, normal and circumferential). This grid resolution is inadequate for numerical simulation of the entire projectile including the base region. In order to obtain meaningful results, computations were carried out in two pieces. The first one corresponds to the solution over the projectile with emphasis on the forebody solution $X/D < 4.5$ and the other, $X/D > 4.5$, containing the boattail corner and the base region. For each of these cases, a 70 X 36 X 21 grid was used. Computations were first run for the projectile where the base flow was modeled as an extended sting.[2] The converged solution at $X/D = 4.5$ was then used as an upstream boundary condition for computation of the boattailed afterbody and base region flow field using the grid shown in Figure 3. The code, however, has been developed so that complete numerical simulation of a projectile including the base region can be made. Such simulations require larger computer memory and are currently in progress using the BRL CRAY X-MP/48 computer.

Particle paths in the base region for both the windward and the leeward planes are shown in Figure 4. This figure shows the general feature of the flow in the base region. The recirculatory flow in the base is evident. In addition, this figure shows the expected asymmetry in the recirculatory flow pattern in the wind-side and the lee-side planes. The size of the separation bubble in the lee-side is much larger than that on the wind-side. Figure 5 shows the grid and the Mach number contours in the same perspective view which includes the windward and leeward planes as well as the circumferential plane at the end of the afterbody, i.e., at the base. As seen in Figure 5a, the grid stretching at the base region in the normal direction is used on both sides of the base corner. The corresponding Mach contours in Figure 5b show the expansion wave front in the base region which seems to grow as the lee-side is approached.

Figures 6 and 7 are two-dimensional views which show the Mach contours and pressure contours, respectively, over the boattail and in the base region for the windward and leeward planes. Figure 6 shows mixed regions of subsonic flow and supersonic flow. The recirculation region in the near wake is subsonic. It also indicates the asymmetry in the flow field in the base region and the presence of strong free shear layers. Pressure contours are shown in Figure 7 which show the expansion at the boattail corner and indicate the presence of a shock wave on the boattail. The grid in the longitudinal direction on the boattail is rather coarse and, thus, a sharp shock wave is not seen. The expected asymmetry in the near wake flow field is clearly seen in this figure. The position of the shock wave is better shown in Figure 8. The shock location is based on looking at the Mach number component in the direction of the local pressure gradient. The shock structure is asymmetric. The shock wave on the boattail in the wind-side is closer to the base than the one in the lee-side.

7

The surface pressure coefficient is shown as a function of the longitudinal position for both the wind-side and the lee-side in Figure 9. The computational results are compared with the experimental data[11] shown in squares and circles. The agreement between the computed surface pressure coefficient and experimental data on the wind-side is good. The expansions and recompressions near the ogive-cylinder and cylinder-boattail junctions are captured adequately by the computation. Comparison of the surface pressure on the lee-side shows discrepancy on the ogive as well as the boattail. The agreement with experimental data is better near the ogive-cylinder junction. The computed surface pressure on the lee-side is lower than that on the wind-side; whereas the reverse is true on the boattail. A similar trend is observed experimentally. Comparisons between computation and experiment for the circumferential surface pressure distribution are shown in Figures 10-13 for longitudinal positions X/D = 4.5, 5.19, 5.56 and 5.78, respectively. Figure 10 shows the comparison at X/D = 4.5. This is on the cylindrical portion upstream of the boattail. The agreement between the computation and experiment is excellent. This solution was used as an upstream boundary condition for the boattailed afterbody and base region flow computation. Comparisons at the next three stations are on the boattail. Figures 11 and 12 show the comparisons at X/D = 5.19 and 5.56, respectively. As seen in these figures, the computation predicts the correct trend of the data. The agreement is good near the wind-side ($\phi = 0$) and gets worse as the lee-side ($\phi = 180°$) is approached (overpredicting at X/D = 5.19 and underpredicting at X/D = 5.56). The next station, X/D = 5.78 is on the boattail just ahead of the base corner (Figure 13) and here the influence of the base region flow should be the largest. Discrepancy between the computed result and the experiment exists at all points in the circumferential direction at this station; however, the trend of data is again correctly captured in the computed result. The discrepancy is partly due to the fact that the experimental data were obtained using a sting mounted model whereas the computation does not include the sting and also partly due to lack of adequate grid resolution on the boattail. The effect that the asymmetrically located shock structure existing on the boattail can have on the pitching moment is not clearly understood and is a subject of further investigation.

The base pressure for this SOCBT projectile has been obtained and plotted as a function of roll angle in Figure 14. The computed result (solid line) is compared to experimental data[12] shown in circles. This base pressure is taken at 44% of the base radius from the center line. As seen in this figure, the base pressure coefficient seem to decrease slightly in going from the wind-side to the lee-side. This trend is also observed in the experiment. The computed result is underpredicted; however, it should be noted that these base pressures were measured with a sting mounted in the base region. The effect of the sting on the base pressure and the boattail flow field has not been modeled in the present computation. In addition, the computational grid in the base region has been severely stretched in the streamwise direction.

The final result desired from the flowfield calculations is the determination of the aerodynamic coefficients. The results to be presented here include the axial force and normal force coefficients. These are obtained by integration of the pressure and viscous forces acting on the projectile. These aerodynamic coefficients are plotted in Figures 15 and 16 as a function of longitudinal position and illustrate the development of the force over the length of the projectile. Figure 15 shows the axial force coefficient as it

begins to rise over the first half of the nose ($P > P_\infty$) and then drop as the ogive-cylinder junction is approached ($P < P_\infty$). This is followed by a sma'l increase over the cylinder which results from the viscous contribution only. There is no contribution to this increase due to the pressure forces on the cylinder. The axial force coefficient rises sharply over the boattail and then levels off. Comparison with the accumulated axial force coefficient obtained experimentally shows favorable agreement. The experimental result does not include the viscous component; and, therfore, is expected to be smaller than the computational result. Figure 16 is a plot of the normal force coefficient. The rapid increase in normal force that occurs on the ogive portion of the projectile is shown. The cylinder portion should produce no significant additional normal force; however, the computation indicates a slight increase in the normal force. The reversal in the direction of the force on the boattail can be seen clearly. The accumulated normal force coefficient, indicated by the dark dot, has been overpredicted by the computation. It is clear that the boattail has a dramatic effect on the aerodynamic coefficients. Thus, good resolution of the boattail flowfield is essential.

VI. CONCLUDING REMARKS

This report described the development and the application of an unsteady, thin-layer, Navier-Stokes base flow code to compute the 3-D base flow of projectiles at transonic speeds.

This capability, which utilizes an implicit finite difference scheme, was used to predict the base region flowfield of a projectile at $M_\infty = .96$ and $\alpha = 4°$. The solution was marched in time for approximately 2800 time steps to obtain the steady state result. Computations were performed on a Cray X-MP/22 computer using 52920 grid points which required 14 hours computer time. Computed results show the recirculation region and the asymmetric wake in the base region. The initial results indicate the presence of asymmetrically located shock structure on the boattail upstream of the base corner. The poor agreement between the computed surface pressures and aerodynamic coefficients with experimental data indicate the need for more grid resolution. These initial results are encouraging and the capability has now been established for three dimensional numerical simulation of a projectile including the base region. The need for additional grid resolution exists for accurate numerical predictions. Accurate prediction of all these coefficients is needed. Further computations are then needed at other Mach numbers in the transonic regime to determine the critical aerodynamic behavior of projectiles.
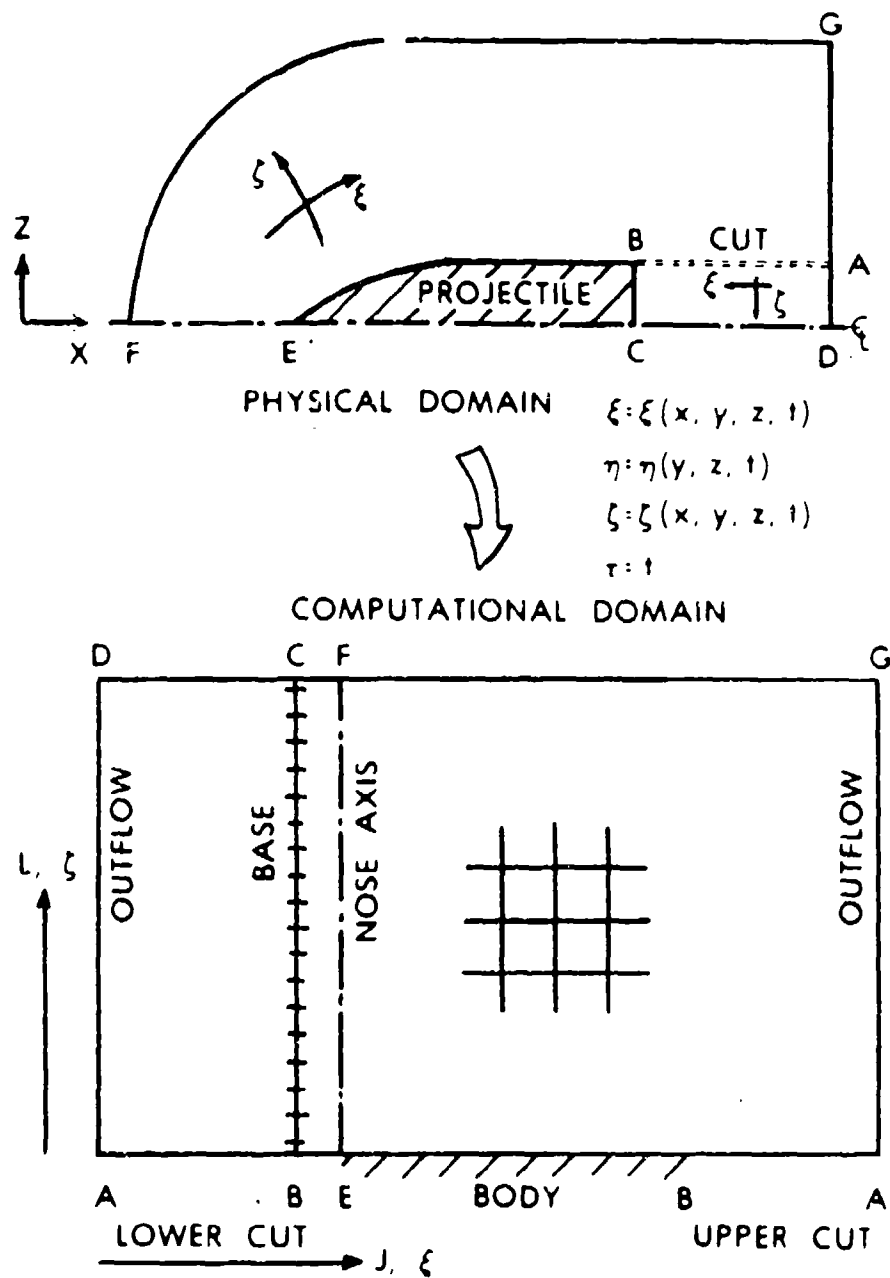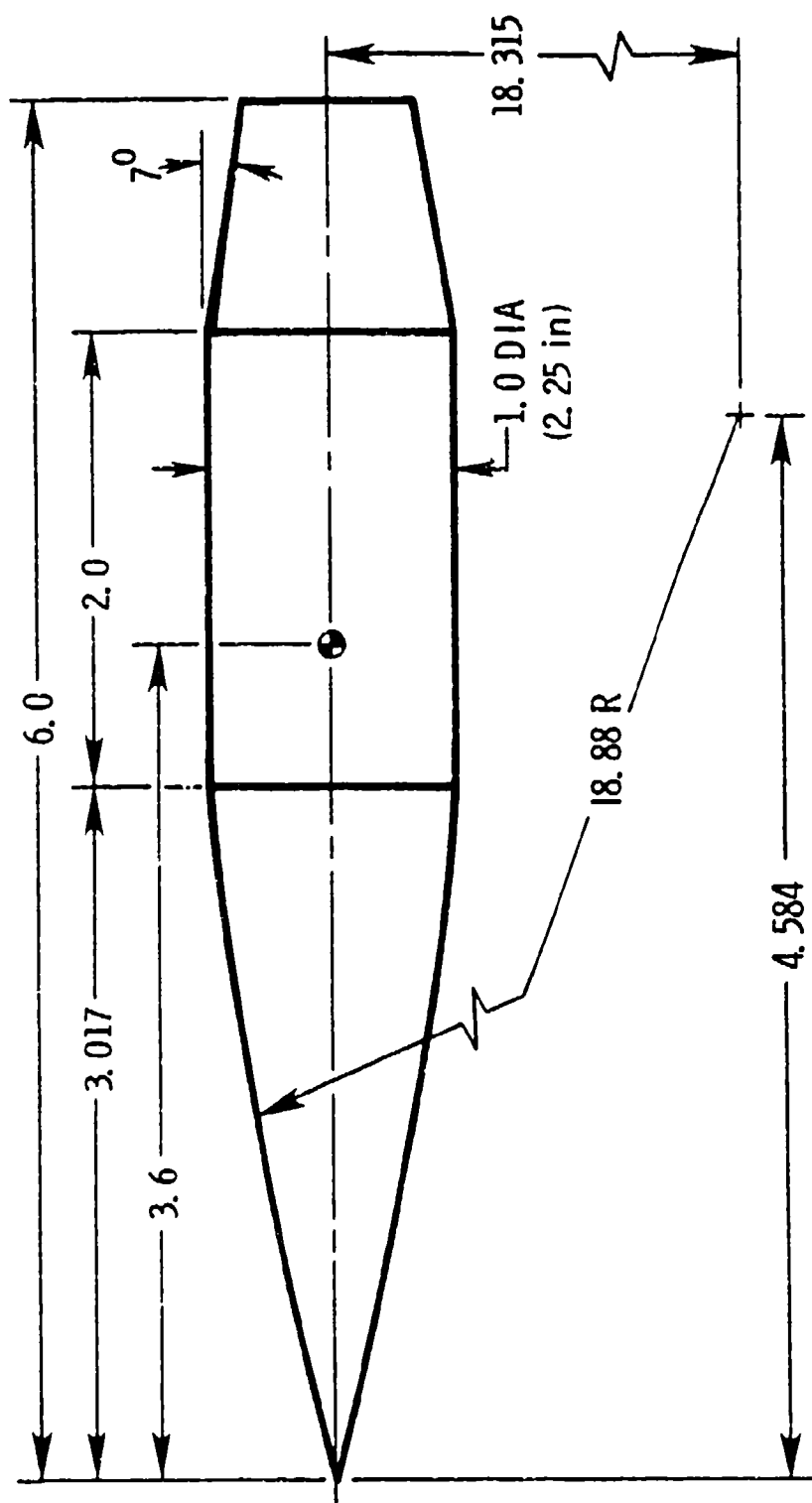
PHYSICAL DOMAIN

$\xi : \xi(x, y, z, t)$

$\eta : \eta(y, z, t)$

$\zeta : \zeta(x, y, z, t)$

$\tau : t$

COMPUTATIONAL DOMAIN

Figure 1. Schematics of flow field segmentation.

SOCBT

ALL DIMENSIONS IN CALIBERS

Figure 2. Details of model geometry.

18.315

7°
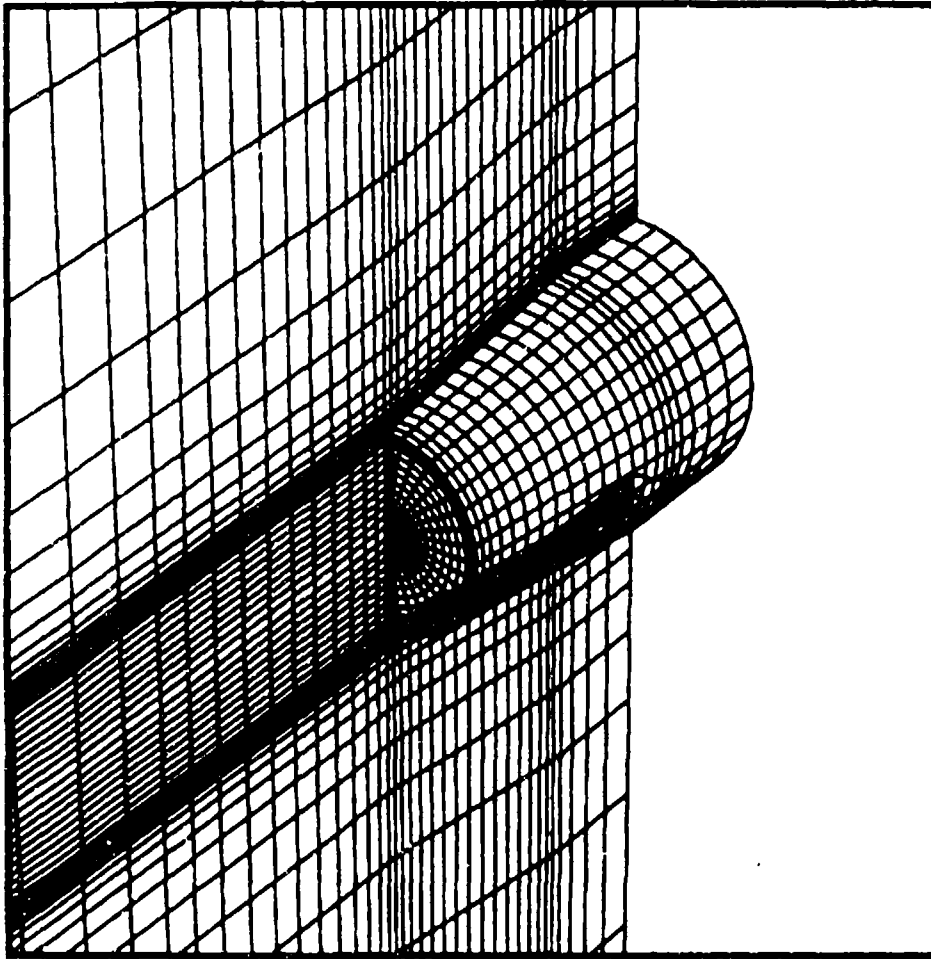
1.0 DIA
(2.25 in)

2.0

6.0

3.017

3.6

18.88 R

4.584

Figure 3. Expanded grid over the boattail and base region.
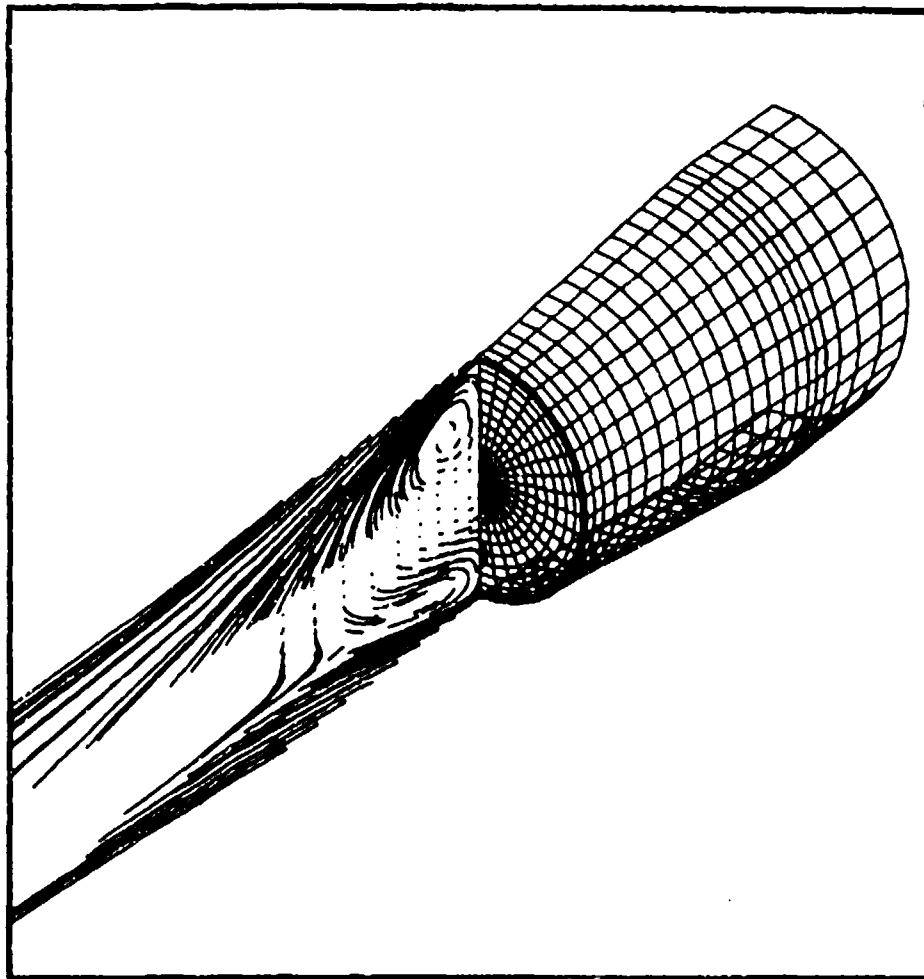
Figure 4. Particle paths in windward and leeward planes in the base region, $M_\infty = .96$, $\alpha = 4°$.
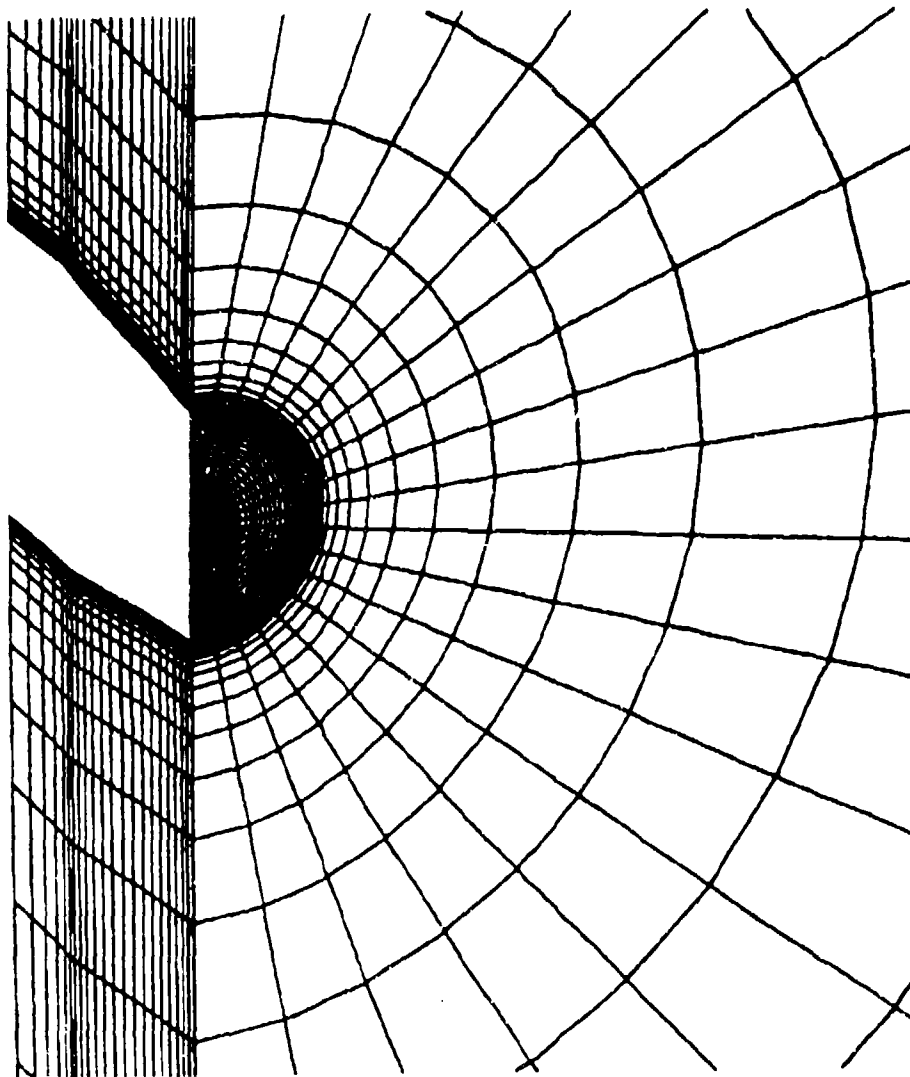
Figure 5a. Computational grids for the wind-side, lee-side and base regions.

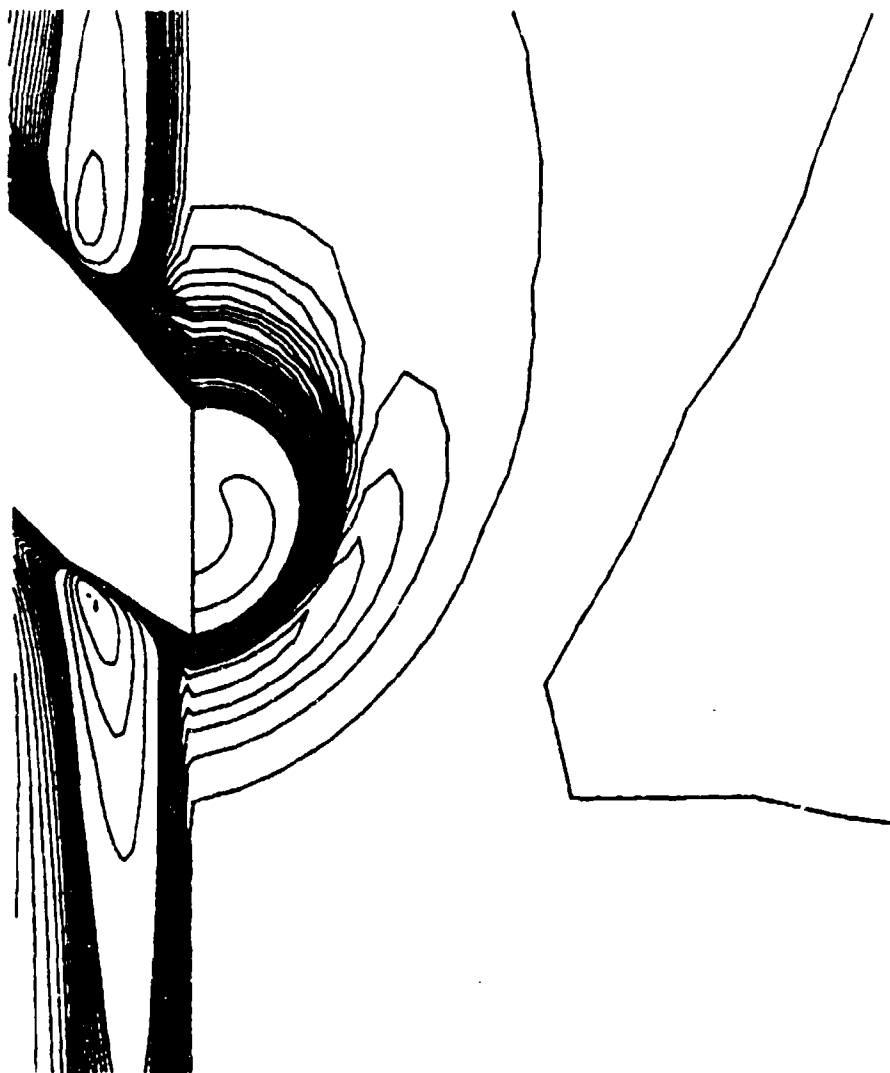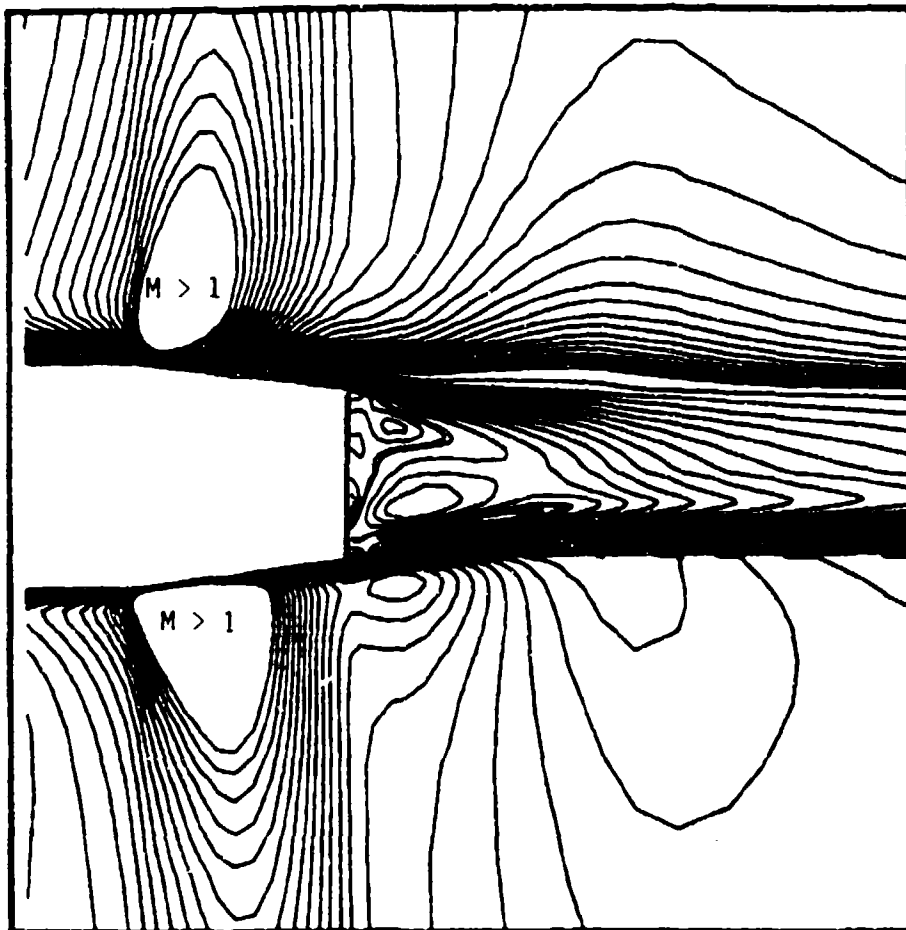Figure 5b. Mach contours for the wind-side, lee-side and base regions, $M_\infty = .96$, $\alpha = 4°$.

Figure 6.   Mach contours in the base region, $M_\infty = .96$, $\alpha = 4°$.

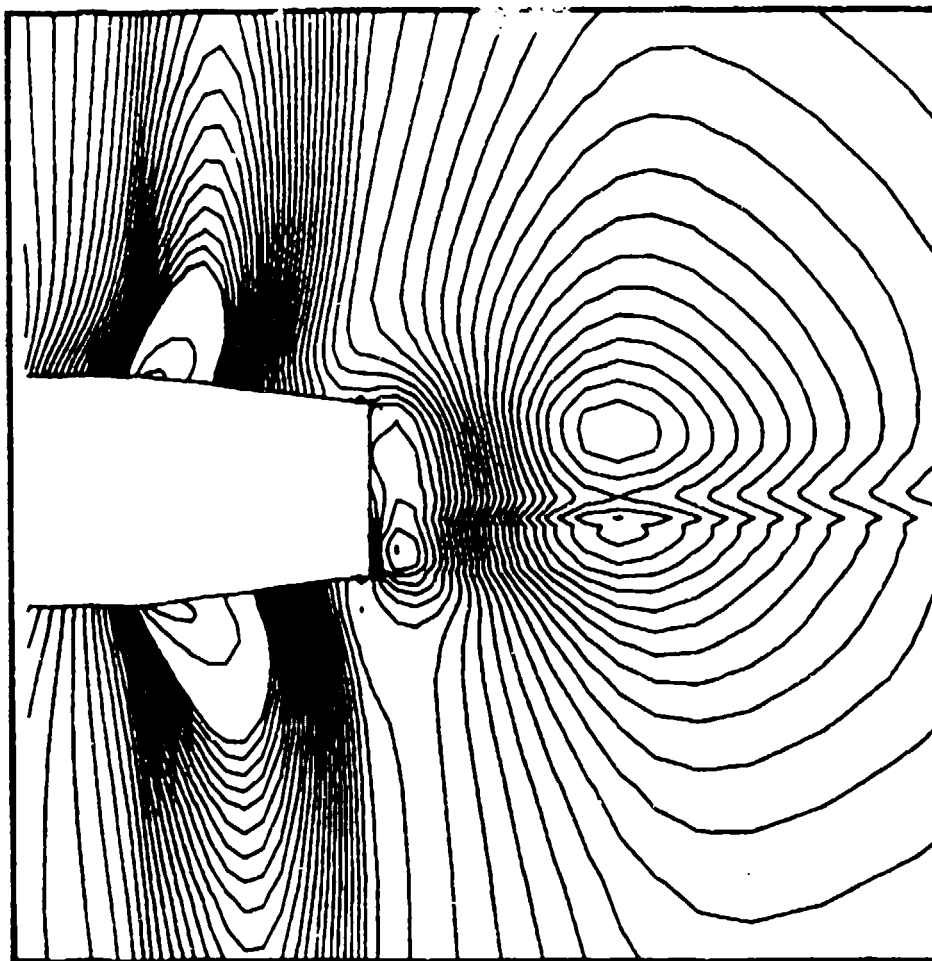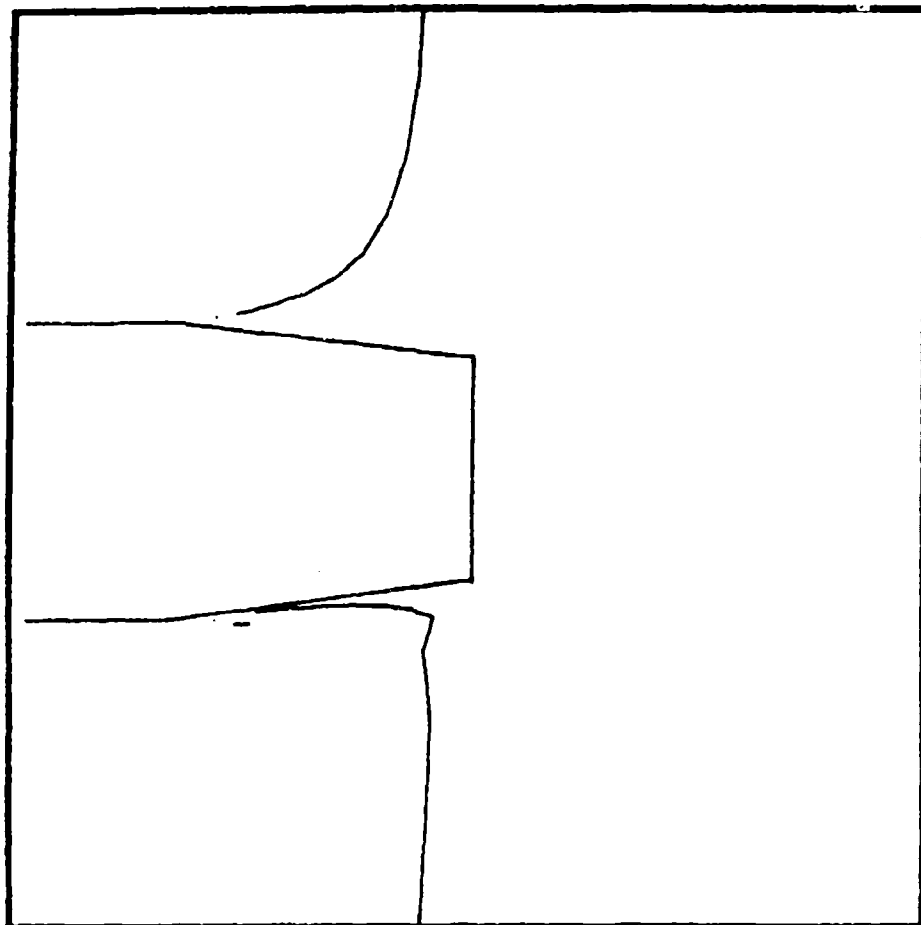Figure 7. Pressure contours in the base region, $M_\infty = .96$, $\alpha = 4°$.

Figure 3. Shock locations on the boattail, $M_\infty = .96$, $\alpha = 4°$.

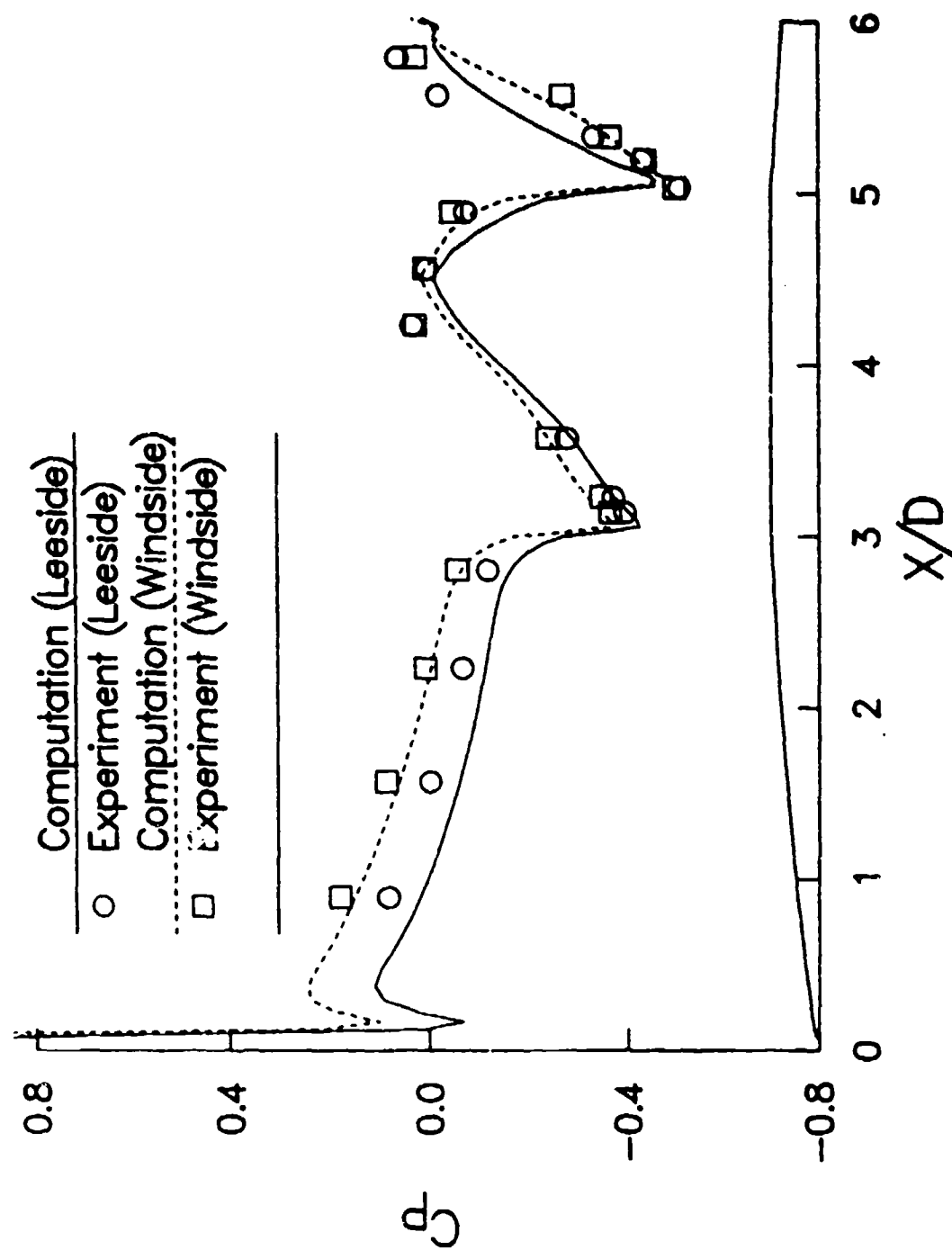Figure 9. Longitudinal surface pressure distribution, $M_\infty = .96$, $\alpha = 4°$.

Figure 10. Circumferential surface pressure distribution, $M_\infty = .96$, $\alpha = 4°$, $X/D = 4.5$.

Figure 11. Circumferential surface pressure distribution, $M_\infty = .96$, $\alpha = 4°$, $X/D = 5.19$.

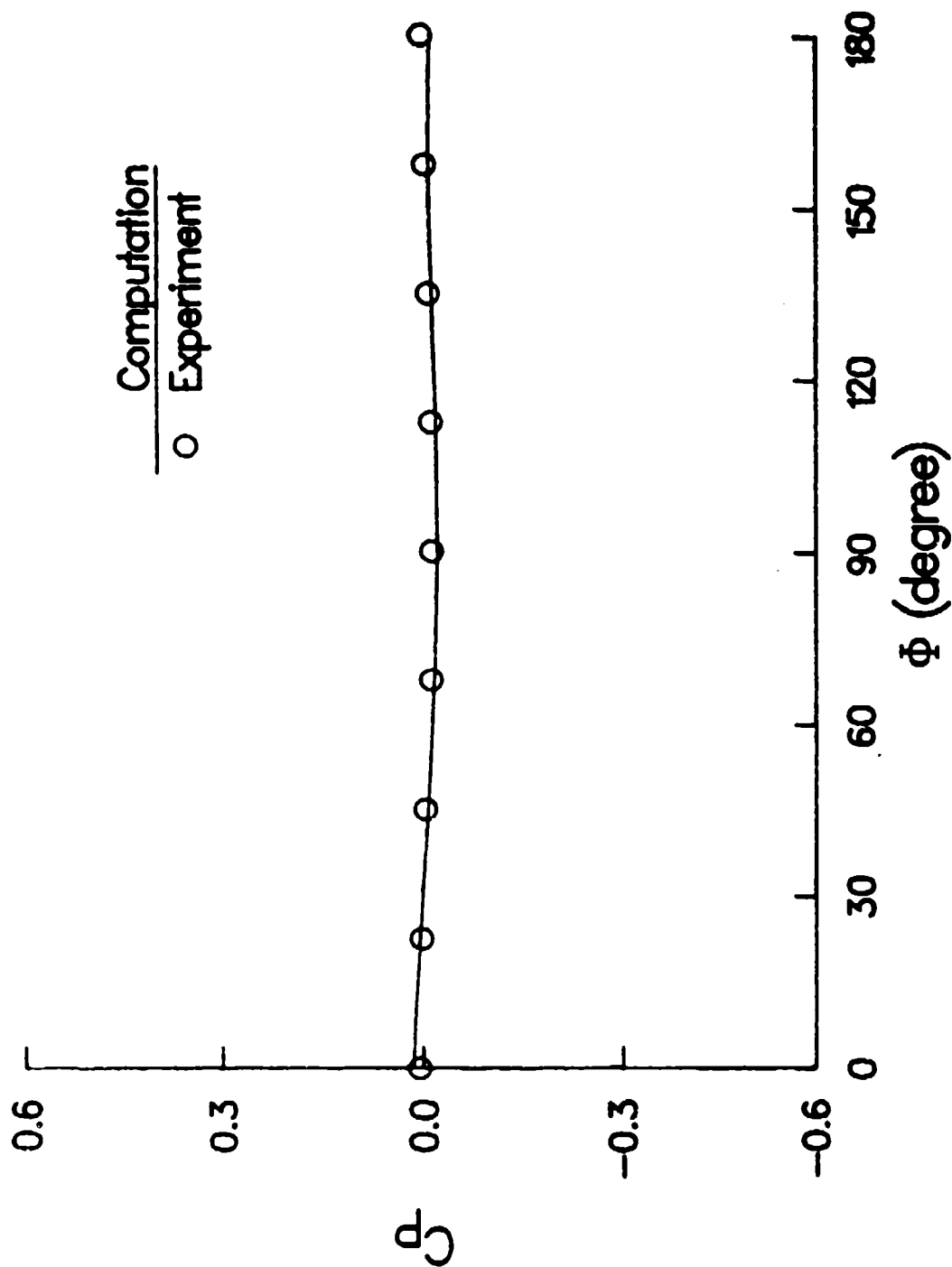Figure 12. Circumferential surface pressure distribution, $M_\infty = .96$, $\alpha = 4°$, $X/D = 5.56$.

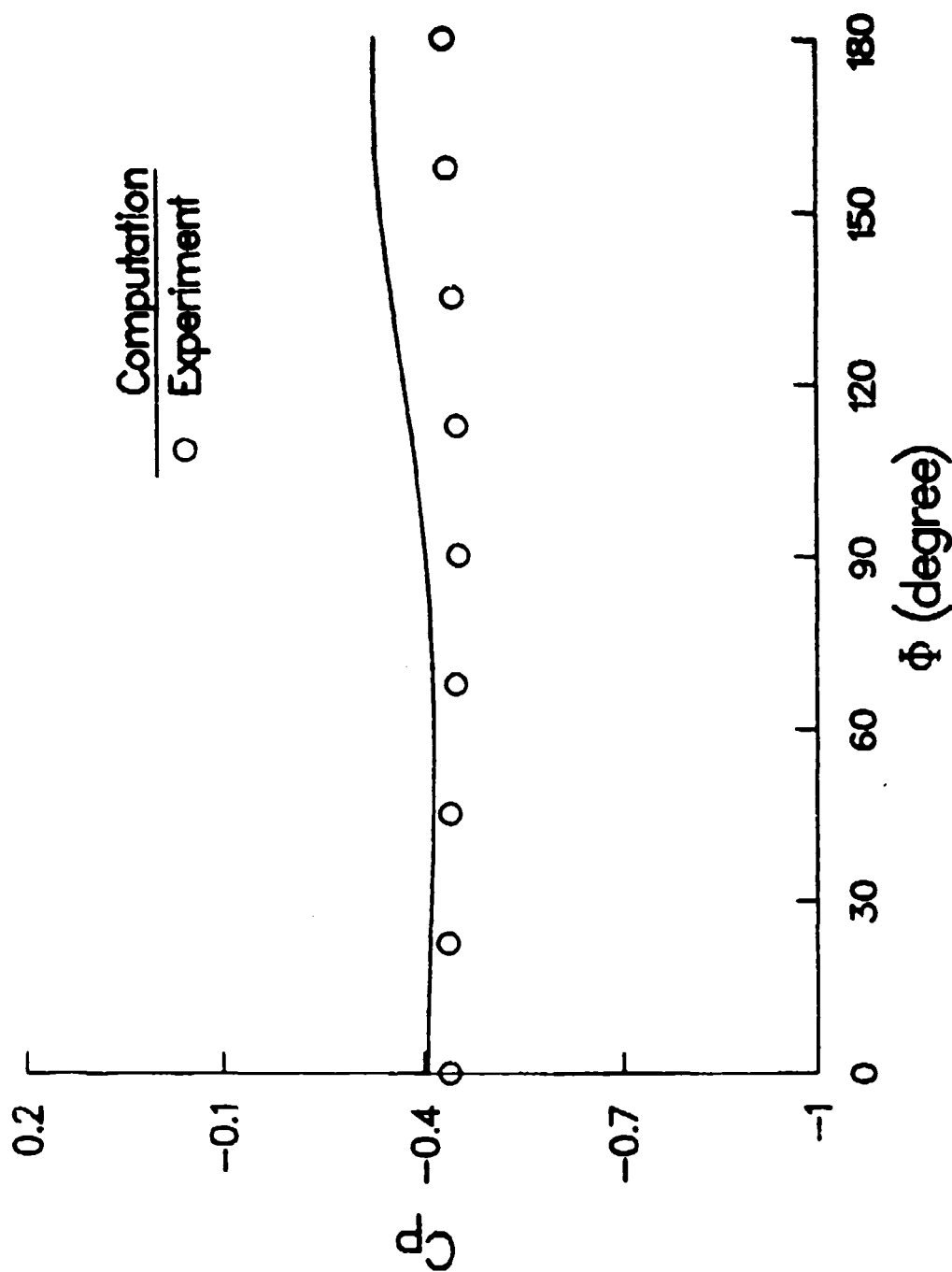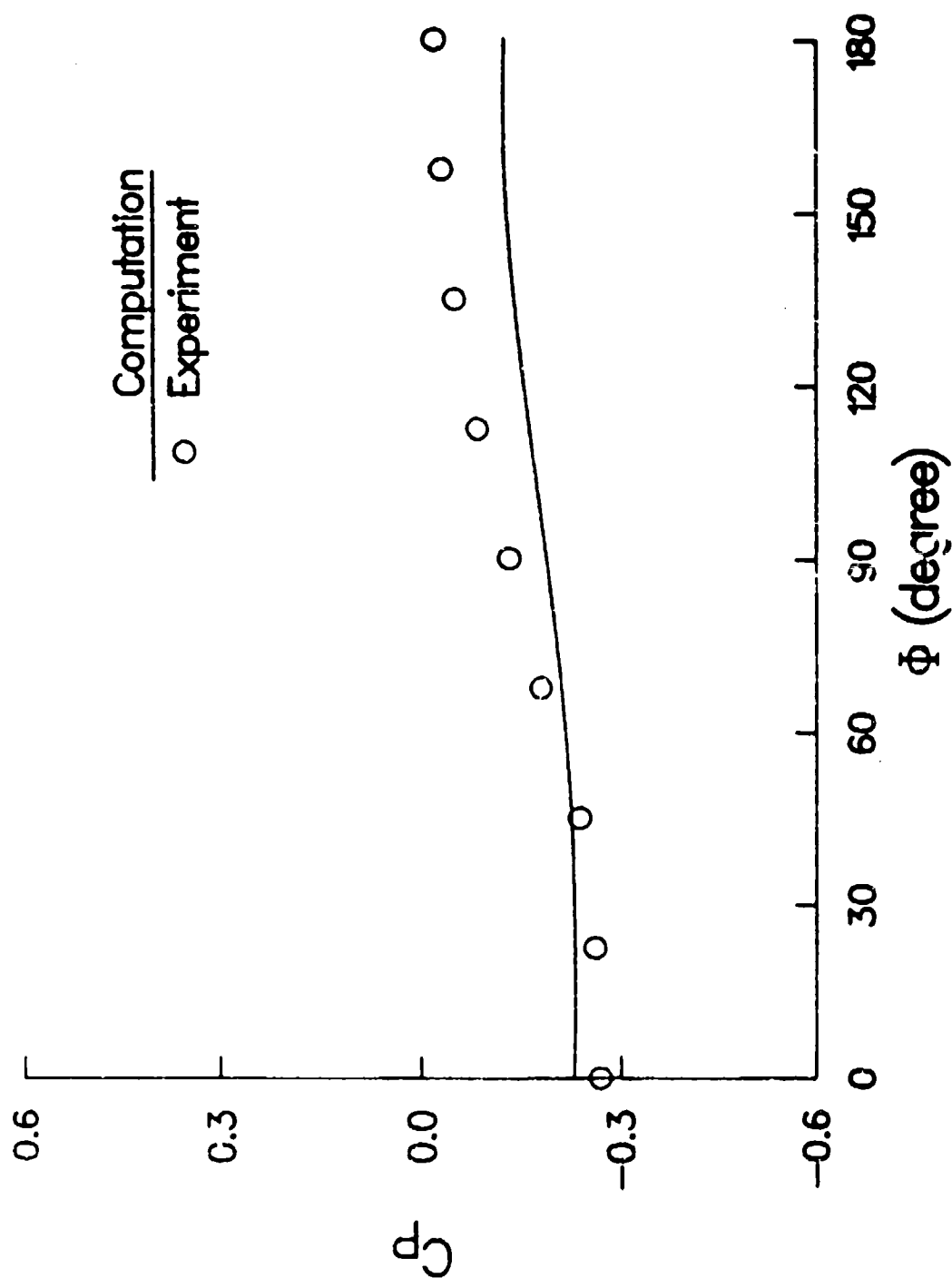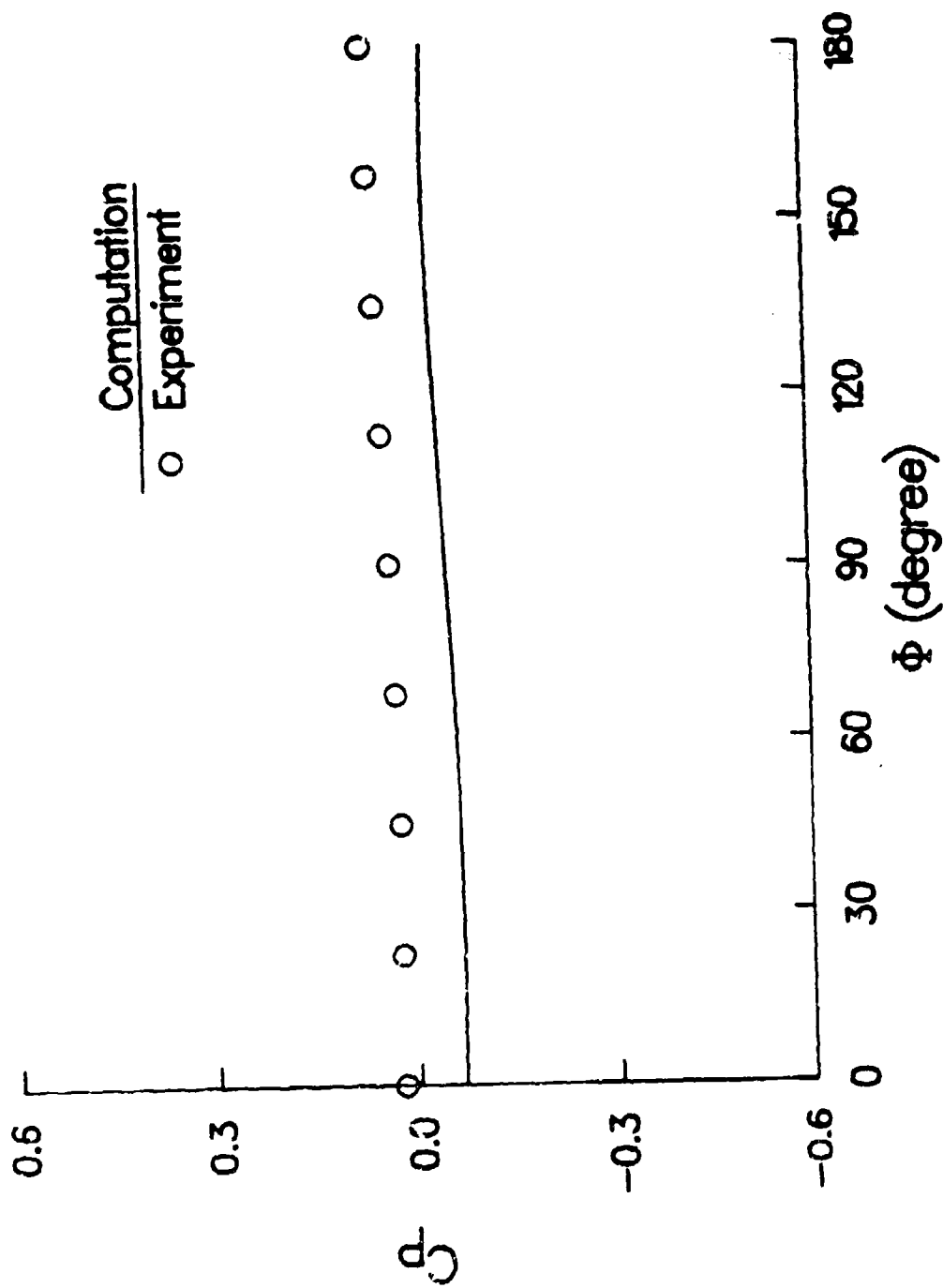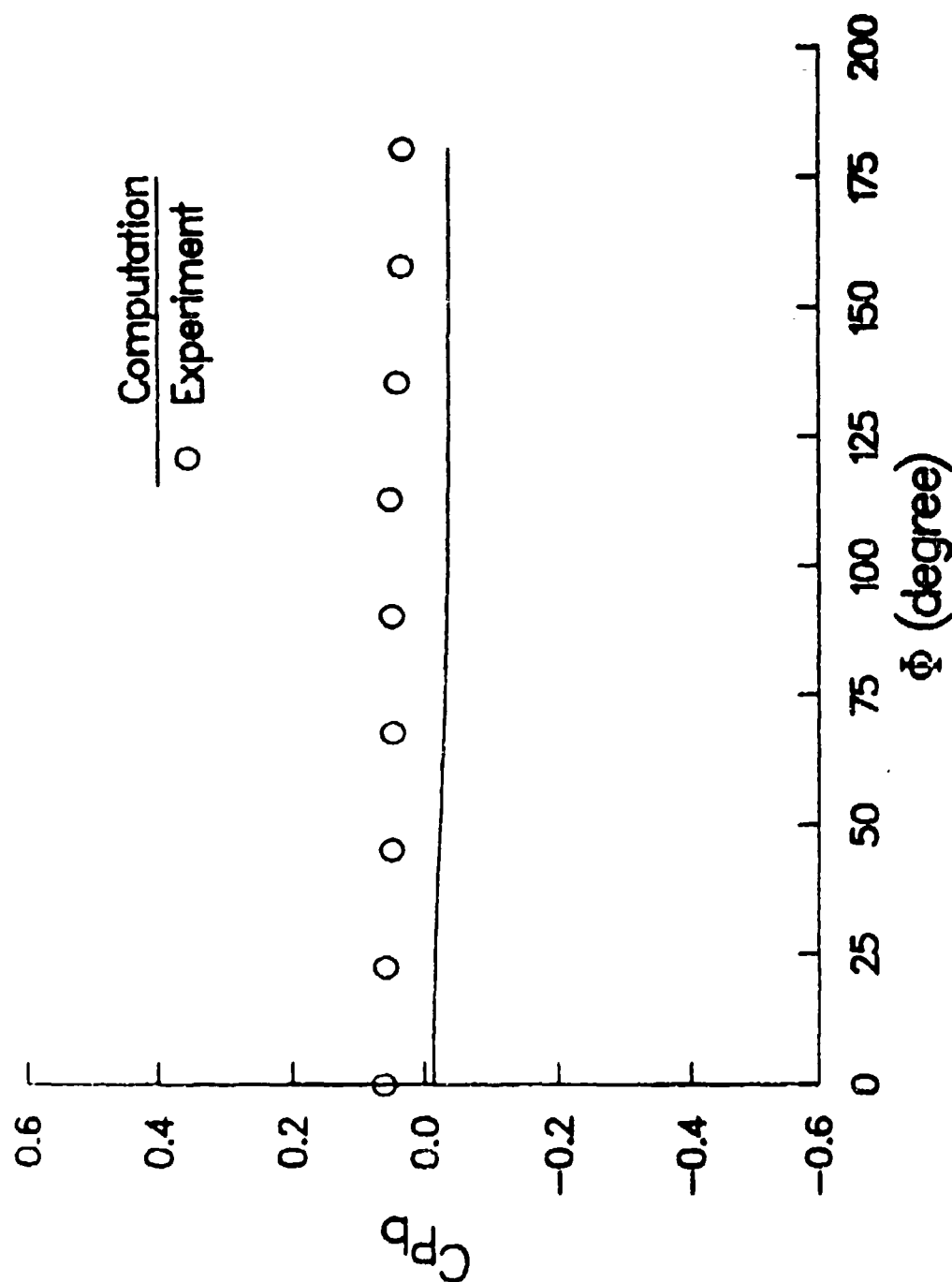Figure 13. Circumferential surface pressure distribution, $M_\infty = .96$, $\alpha = 4°$, $X/D = 5.78$.

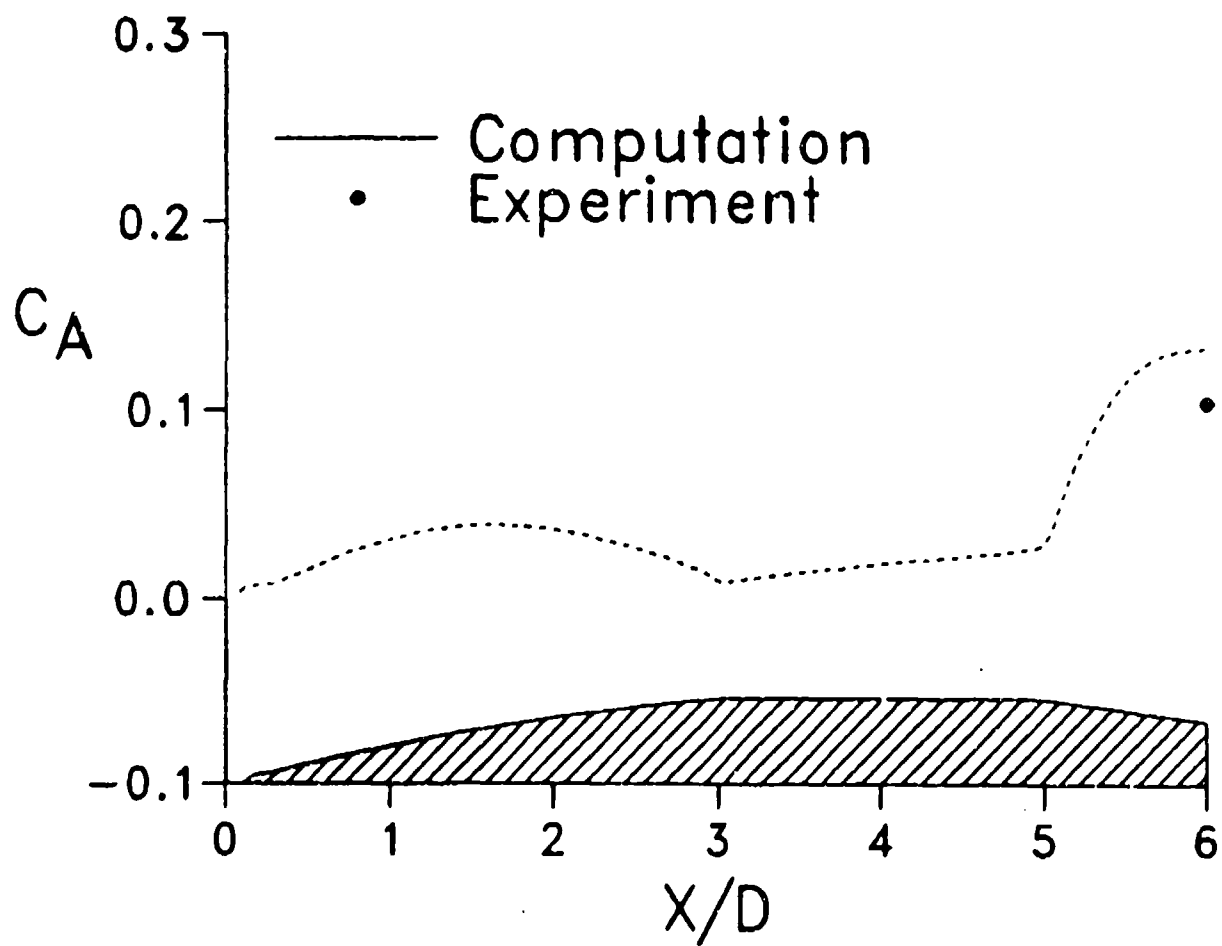Figure 14. Circumferential base pressure distribution, $M_\infty = .96$, $\alpha = 4°$.

24

Figure 15. Development of axial force coefficient over the projectile, $M_\infty = .96$, $\alpha = 4°$.
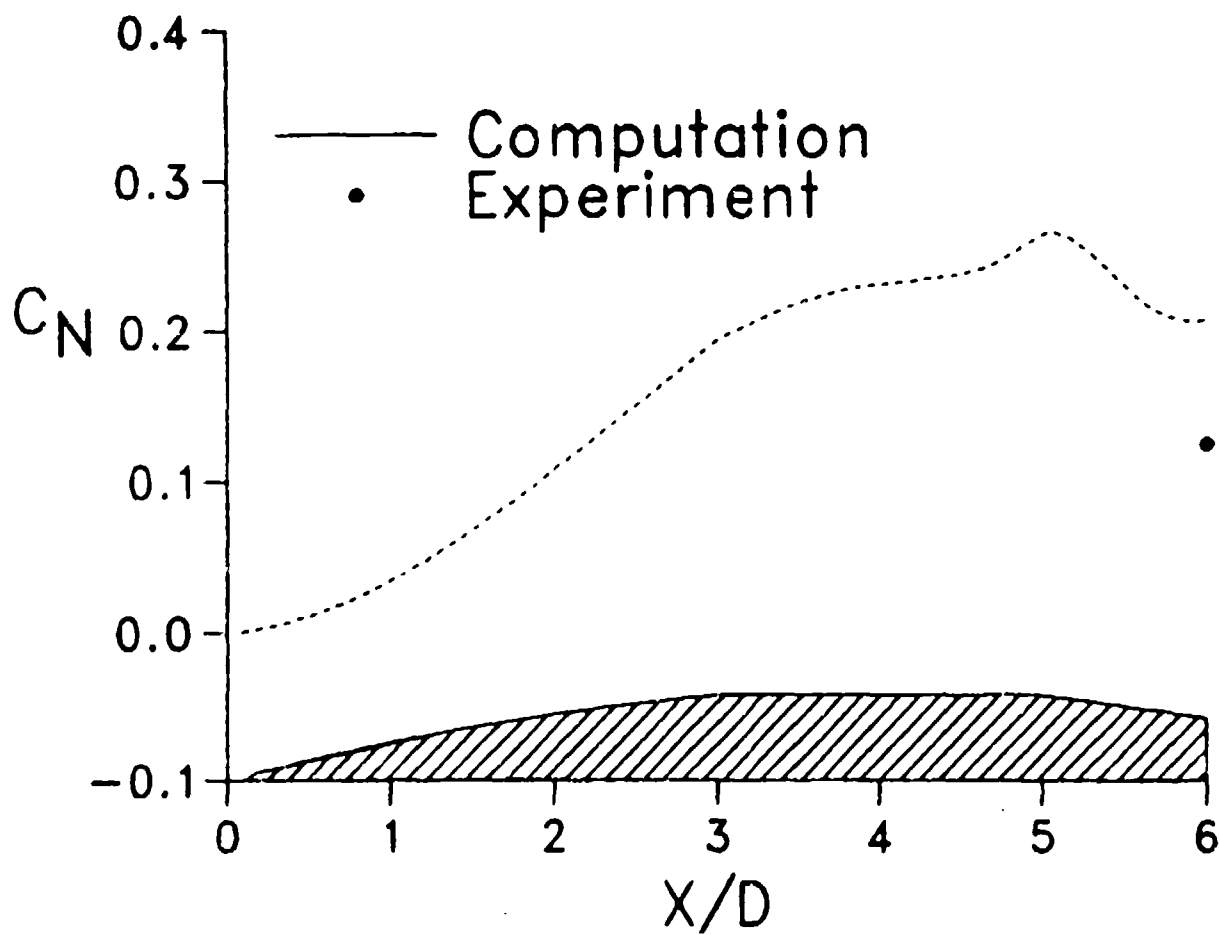
Figure 16. Development of normal force coefficient over the projectile, $M_\infty = .96$, $\alpha = 4°$.

REFERENCES

1. Nietubicz, C.J., Pulliam, T.H. and Steger, J.L., "Numerical Solution of the Azimuthal-Invariant Thin-Layer Navier-Stokes Equations," ARBRL-TR-02227, US Army Ballistic Research Laboratory, Aberdeen Proving Ground, Maryland, March 1980. (AD A085716) (Also see AIAA Journal, Vol. 18, No. 12, December 1980, pp. 1411-1412.)

2. Nietubicz, C.J., Sturek, W.B. and Heavey, K.R., "Computations of Projectile Magnus Effect at Transonic Velocities," AIAA Journal, Vol. 23, No. 7, July 1985.

3. Deiwert, G.S., "Numerical Simulation of Three Dimensional Boattail Afterbody Flow Field," AIAA Journal, Vol. 19, May 1981, pp. 582-588.

4. Sahu, J., Nietubicz, C.J. and Steger, J.L., "Navier-Stokes Computations of Projectile Base Flow with and without Mass Injection," ARBRL-TR-02532, US Army Ballistic Research Laboratory, Aberdeen Proving Ground, Maryland, November 1983. (AD A135738) (Also see AIAA Journal, Vol. 23, No. 9, September 1985.)

5. Sahu, J., "Computations of Supersonic Flow over a Missile Afterbody Containing an Exhaust Jet," AIAA Paper No. 85-1815-CP, August 1985.

6. Baldwin, B.S. and Lomax, H., "Thin-Layer Approximation and Algebraic Model for Separated Turbulent Flows," AIAA Paper No. 78-257, 1978.

7. Pulliam, T.H. and Steger, J.L., "On Implicit Finite-Difference Simulations of Three-Dimensional Flow," AIAA Journal, Vol. 18, No. 2, February 1980, pp. 159-167.

8. Beam, R. and Warming, R.F., "An Implicit Factored Scheme for the Compressible Navier-Stokes Equations," AIAA Paper No. 85-1815-CP, August 1985.

9. Steger, J.L., "Implicit Finite Difference Simulation of Flow About Arbitrary Geometries with Application to Airfoils," AIAA Journal, Vol. 16, No. 4, July 1973, pp. 679-686.

10. Petrie, H.L. and Walker, B.J., "Comparison of Experiment and Computation for a Missile Base Region Flow Field with a Centered Propulsive Jet," AIAA Paper No. 85-1618, July 1985.

11. Kayser, L.D. and Whiton, F., "Surface Pressure Measurement on a Boattailed Projectile Shape at Transonic Speeds," U.S. Army Ballistic Research Laboratory, Aberdeen Proving Ground, Maryland, ARBRL-MR-03161, March 1982. (AD A113520)

12. Kayser, L.D., "Base Pressure Measurements on a Projectile Shape at Mach Numbers from 0.91 to 1.20," U.S. Army Ballistic Research Laboratory, Aberdeen Proving Ground, Maryland, ARBRL-MR-03353, April 1984. (AD A141341)

13. Steger, J.L., Nietubicz, C.J. and Heavey, K.R., "A General Curvilinear Grid Generation Program for Projectile Configurations," U.S. Army Ballistic Research Laboratory, Aberdeen Proving Ground, Maryland, ARBRL-MR-03142, October 1981. (AD A107334)

LIST OF SYMBOLS

a	=	maximum speed of sound
A	=	cross sectional area
c_p	=	specific heat at constant pressure
C_A	=	axial force coefficient excluding base drag
C_m	=	pitching moment coefficient
C_N	=	normal force coefficient
C_p	=	pressure coefficient, $2(p-p_\infty)/\rho_\infty u_\infty^2$
D	=	body diameter (57.15mm)
e	=	total energy per unit volume/$\rho_\infty a_\infty^2$
$\hat{E}, \hat{F}, \hat{G}$	=	flux vector of transformed Navier-Stokes equations
J	=	Jacobian of transformation
M	=	Mach number
p	=	pressure/$\rho_\infty a_\infty^2$
Pr	=	Prandtl number, $\mu_\infty c_p/\kappa_\infty$
$\hat{q}$	=	vector of dependent variables
R	=	body radius
Re	=	Reynolds number, $\rho_\infty a_\infty D/\mu_\infty$
$\hat{S}$	=	viscous flux vector
t	=	physical time
u,v,w	=	Cartesian velocity components/a_∞
U,V,W	=	Contravariant velocity components/a_∞
x,y,z	=	physical Cartesian coordinates
α	=	angle of attack
γ	=	ratio of specific heats
κ	=	coefficient of thermal conductivity
μ	=	coefficient of viscosity

29

LIST OF SYMBOLS   (Continued)

ξ, η, ζ = transformed coordinates in axial, circumferential and radial directions

ρ = density/ρ_∞

τ = transformed time

ϕ = circumferential angle

Superscript

$*$ = critical value

Subscript

b = base

∞ = free stream conditions

DISTRIBUTION LIST

No. of Copies	Organization	No. of Copies	Organization
12	Administrator Defense Technical Info Center ATTN: DTIC-FDAC Cameron Station, Bldg 5 Alexandria, VA 22304-6145	1	Director US AMCCOM ARDEC CCAC Benet Weapons Laboratory ATTN: SMCAR-CCB-TL Watervliet, NY 12189-4050
1	HQDA DAMA-ART-M Washington, DC 20310	1	Commander US Army Aviation Systems Cmd ATTN: AMSAV-E 4300 Goodfellow Blvd. St. Louis, MO 63120-1798
1	Commander US Army Materiel Command ATTN: AMCDRA-ST 5001 Eisenhower Avenue Alexandria, VA 22333-0001	1	Director US Army Aviation Research & Technology Activity Ames Research Center Moffett Field, CA 94035-1099
4	Commander Armament RD&E Center US Army AMCCOM ATTN: SMCAR-MSI SMCAR-LCA-F/Klein Loeb Hudgins Dover, NJ 07801-5001	3	Commander US Army Missile Command ATTN: AMSMI-RX Redstone Arsenal, AL 35898-5249
1	Commander US Army Armament, Munitions & Chemical Command ATTN: SMCAR-IMP-L Rock Island, IL 61299-7300	1	Director US Army Missile & Space Intelligence Center ATTN: AIAMS-YDL Redstone Arsenal, AL 35898-5500
1	Commander US Army Armament, Research, Development & Engineering Ctr ATTN: SMCAR-TDC Dover, NJ 07801	1	Commander US Army Tank Automotive Command ATTN: AMSTA-TSL Warren, MI 48397-5500
1	Commander US Army Jefferson Proving Ground Materiel Testing Directorate ATTN: Arthur B. Alphin, MAJ, ARM Madison, IN 47250-5100	1	Director US Army TRADOC Analysis Center ATTN: ATOR-TSL White Sands Missile Range, NM 88002-5502
1	Commander CECOM R&D Technical Library ATTN: AMSEL-IM-L Fort Monmouth, NJ 07703-5000	1	Commander US Army Research Office P. O. Box 12211 Research Triangle Park, NC 27709

No. of Copies	Organization
1	Commander US Naval Air Systems Command ATTN: AIR-604 Washington, DC 20360
2	Commander US Naval Surface Weapons Center ATTN: Dr. T. Clare, Code DK20 Dr. F. Moore Dahlgren, VA 22448-5000
1	Commander US Naval Weapons Center ATTN: Code 3431, Tech Lib China Lake, CA 93555
1	Commander US Army Development & Employment Agency ATTN: MODE-ORO Ft. Lewis, WA 98433-5000
1	Director NASA Langley Research Center ATTN: NS-185, Tech Lib Langley Station Hampton, VA 23365
4	Director NASA Ames Research Center ATTN: MS-202-1/Pulliam MS-258-1/Steger Schiff Jettmar Moffett Field, CA 94035
2	Commandant US Army Infantry School ATTN: ATSH-CD-CS-OR Ft. Benning, GA 31905
1	Commandant USAFAS ATTN: ATSF-TSM-CN Ft. Sill, OK 73503-5600
1	AFWL/SUL Kirtland AFB, NM 87117

No. of Copies	Organization
1	AFATL/DOIL (Tech Info Ctr) Eglin AFB, FL 32542-5438
2	Sandia Laboratories ATTN: Dr. W.L. Oberkampf Dr. F. Blottner Division 1636 Sandia National Laboratories Albuquerque, NM 87185
1	AEDC Calspan Field Services ATTN: MS 600 (Dr. John Benek) AAFS, TN 37389
1	Virginia Polytechnic Institute & State University ATTN: Dr. Clark H. Lewis Department of Aerospace & Ocean Engineering Blacksburg, VA 24061
1	University of California, Davis Department of Mechanical Engineering ATTN: Prof. H.A. Dwyer Davis, CA 95616
1	Pennsylvania State University Department of Aerospace Engineering ATTN: Dr. G. S. Dulikravich University Park, PA 16802
1	University of Florida Dept. of Engineering Sciences College of Engineering ATTN: Prof. C. C. Hsu Gainesville, FL 32611
10	CIA OIR/DB/Standard GE47 HQS Washington, DC 20505

DISTRIBUTION LIST

No. of
Copies   Organization

1   University of Illinois
            at Urbana Champaign
        Department of Mechanical &
            Industrial Engineering
        ATTN: Prof. W. L. Chow
        Urbana, IL 61801

1   University of Maryland
        Department of Aerospace Engineering
        ATTN: Dr. J.D. Anderson, Jr.
        College Park, MD 20742

1   University of Notre Dame
        Department of Aeronautical
            & Mechanical Engineering
        ATTN: Prof. T.J. Mueller
        Notre Dame, IN 46556

1   University of Texas
        Department of Aerospace Engineering
            & Engineering Mechanics
        ATTN: Dr. D.S. Dolling
        Austin, Texas 78712-1055

Aberdeen Proving Ground

Dir, USAMSAA
   ATTN: AMXSY-D
          AMXSY-MP, H. Cohen

Cdr, USATECOM
   ATTN: AMSTE-SI-F

Cdr, CRDEC, AMCCOM
   ATTN: SMCCR-RSP-A
          SMCCR-MU
          SMCCR-SPS-IL

USER EVALUATION SHEET/CHANGE OF ADDRESS

This Laboratory undertakes a continuing effort to improve the quality of the reports it publishes. Your comments/answers to the items/questions below will aid us in our efforts.

1. BRL Report Number_____Date of Report_____

2. Date Report Received_____

3. Does this report satisfy a need? (Comment on purpose, related project, or other area of interest for which the report will be used.)_____

_____

_____

4. How specifically, is the report being used? (Information source, design data, proc 're, source of ideas, etc.)_____

_____

_____

5. Has the information in this report led to any quantitative savings as far as man-hours or dollars saved, operating costs avoided or efficiencies achieved, etc? If so, please elaborate._____

_____

_____

6. General Comments. What do you think should be changed to improve future reports? (Indicate changes to organization, technical content, format, etc.)

_____

_____

_____

	Name
CURRENT ADDRESS	Organization
	Address
	City, State, Zip

7. If indicating a Change of Address or Address Correction, please provide the New or Correct Address in Block 6 above and the Old or Incorrect address below.

	Name
OLD ADDRESS	Organization
	Address
	City, State, Zip

(Remove this sheet, fold as indicated, staple or tape closed, and mail.)